

An Experimental Method to Determine the Tensile Strength of Concrete at High Rates of Strain

B. Erzar · P. Forquin

Received: 16 January 2009 / Accepted: 11 August 2009 / Published online: 19 September 2009
© Society for Experimental Mechanics 2009

Abstract In the present work, dynamic tensile strength of concrete is experimentally investigated by means of spalling tests. Based on extensive numerical simulations, the paper presents several advances to improve the processing of spalling tests. The striker is designed to get a more uniform tensile stress field in the specimen. Three methods proposed in the literature to deduce the dynamic strength of the specimen are discussed as well as the use of strain gauges and a laser extensometer. The experimental method is applied to process data of several tests performed on wet micro-concrete at strain rates varying from 30 to 150/s. A significant increase of the dynamic tensile strength with strain-rate is observed and compared with data of the literature. In addition, post-mortem studies of specimens are carried to improve the analysis of damage during spalling tests.

Keywords Mortar and concrete · Dynamic fragmentation · Spall strength · Hopkinson bar · Strain-rate sensitivity

Introduction

Concrete is a material widely used in structures such as bridges, nuclear power stations or bunkers. These structures can be exposed to intensive dynamic loadings such as industrial accidents or projectile-impacts. Consequently, the knowledge of the tensile behaviour of concrete subjected to high strain-rates is essential. Numerous studies have been carried out in the past to characterise the quasi-static and

dynamic mechanical behaviour and the fracture properties of concrete [1–3]. Toutlemonde [4] performed direct tensile tests with a hydraulic device to study the tensile strength of various concretes over a wide range of strain-rates ($10^{-6}/s$ - $1/s$). On the one hand, Toutlemonde [4] observed a weak influence of aggregate size and water to cement ratio on the increase of strength with strain-rate. On the other hand, an important increment of strength (about 4 to 5 MPa) was observed over the considered range of loading-rate with wet specimens whereas a very limited rate-effect was noted with dry specimens (less than 1 MPa over the same range). The author explained the influence of free water content as a consequence of the Stefan effect [5]. Another experimental device was used by Körmeling et al. [6] and Zielinski [7] based on the principle of split Hopkinson pressure bars (i.e. specimen put in-between the input and output bars). This technique allowed for strain-rate levels up to 1.5/s. Other workers studied the behaviour of concrete in tension at higher loading rates by the so-called spalling technique. The originality of this method is that the specimen-equilibrium is never reached; a compressive pulse is generated by an impact or blasting on one side of the specimen. When it reaches the opposite free end, a tensile reflected pulse propagating in the opposite direction is induced. Both signals (i.e. incident and reflected) superimpose generating a dynamic tensile loading in the core of the specimen. This technique was employed by McVay [8] who subjected reinforced concrete slabs to spalling using an explosive loading. More recently, Klepaczko and Brara [9] applied the spalling technique to a micro-concrete using an instrumented Hopkinson bar made of aluminium alloy. The authors reported Dynamic Increase Factors (DIFs: ratio of dynamic strength to quasi-static strength) up to 13 for wet specimens, and 7.5 for dry ones at strain rates up to $120 s^{-1}$ (the quasi-static strength of wet and dry samples being

B. Erzar · P. Forquin (✉)
Laboratoire de Physique et de Mécanique des matériaux,
Université Paul Verlaine de Metz,
Ile du Saulcy,
57045 Metz Cedex 1, France
e-mail: pascal.forquin@univ-metz.fr

5.0 MPa and 4.0 MPa resp.). The main drawback of the applied method is that it does not use any measurement on the concrete specimen. First, the transmitted pulse is rebuilt from the incident and reflected signals measured on the Hopkinson bar. Then, the elastic stress field in the specimen is reconstructed. Finally, the strength of concrete is deduced from the separation velocity of fragments or from the position of the fracture surface. Schuler et al. [10] also applied the spalling technique but they measured the particle velocity on the free end of the concrete specimen with an accelerometer glued on it. As explained below, these data are used in a formula introduced by Novikov et al. [11] to determine the ultimate strength of the tested concrete. Using this method, DIFs of 4 to 5.5 were obtained at strain rates ranging between 10 and 100/s (the mean value of the quasi-static tensile strength being: 3.24 MPa). Vegt and Weerheijm [12], and Weerheijm and Van Doormaal [13] used a steel Hopkinson bar dynamically loaded by a small detonation charge. The spall strength and fracture energy of concrete were deduced from data of strain gauges put on the specimen beyond the failure zone. At the maximum strain-rate (about 23/s), Weerheijm and Van Doormaal measured a DIF of 5.3 [13] (the quasi-static tensile strength of the tested concrete was 3.0 MPa). However, the dimensions of the input bar (length: 5.5 m, diameter: 75 mm) favour the wave dispersion phenomenon that probably limits the maximum loading rate available in the specimen.

In the present contribution, a new experimental device is proposed that possesses several features of the previous works. A Hopkinson bar made of aluminium alloy is used to reduce the difference of impedance with concrete specimens. Moreover, specific projectiles were designed to improve the homogeneity of tensile loading in the specimen without excessive limitation of the strain rate level. Strain gauges and laser extensometers are also utilized to deduce one by one the wave speed in the specimen, the dynamic Young's modulus, the failure time, the strain-rate in the damaged zone and the dynamic strength of the tested concrete. Furthermore, three methods to determine the tensile strength are discussed by means of numerical simulations involving a single fracture plane or an anisotropic damage model and post mortem observations. The methodology is explained below.

Discussion of the Experimental Method

Concrete Composition and Basic Mechanical Properties

MB50 micro-concrete is an interesting candidate for testing as it has been already used in numerous experimental works. For example, its tensile strength has been measured

in direct tensile tests [4, 5], in bending tests [14] and in splitting tests [15]. The compressive behaviour was observed in simple compression [16] and under high confining pressures [17–20]. The distribution of aggregates was designed to make it representative of a standard concrete but with a smaller maximum grain size (less than 5 mm) that allows one to test it at a reduced scale. Composition and several basic mechanical properties are gathered in Table 1. Quasi-static tensile and compressive tests have been conducted in LPMM. With a tensile strength of 3.7 MPa and a compressive strength of 45.6 MPa wet MB50 shows similar properties to that of a standard concrete. The specimens used for spalling tests are cylinders 46 mm in diameter and 120 or 140 mm in length. They were drilled from large concrete blocks (30×30×20 cm³), cut and ground. During these three machining phases, water was used as a coolant to prevent local overheating of the specimens that could have damaged them. In order to avoid the dissolution of portlandite in water, all the samples were stored in water saturated by lime. Less than one hour before the spalling test, each “saturated” specimen was picked-up from water, its surface was sponge up. Next, strain gages were quickly glued and the specimen was placed beside the Hopkinson bar.

Experimental Device and Instrumentation

The experimental device used for the present spalling tests is shown in Fig. 1. The basic setup consists of a projectile, a Hopkinson bar and a concrete specimen. The impact of the projectile generates an incident compression wave that travels along the bar. At the bar-specimen interface, a part of the signal is transmitted to the concrete cylinder; the other part is reflected back into the bar. The transmitted compressive pulse ($\sigma_c = f(x - C_0 \cdot t)$ in Fig. 2, C_0 being the one-dimensional wave velocity in the specimen) propagates

Table 1 Composition and mechanical properties of the MB50 microconcrete

| Composition of MB50 [4] | |
|---|-------|
| Sand (kg/m ³) | 1,783 |
| Cement (kg/m ³) | 400 |
| Water (kg/m ³) | 200 |
| Admixture (kg/m ³) | 12 |
| Water/Cement | 0.5 |
| Maximum grain size (mm) | 5 |
| Quasi-static strength of wet MB50 (strain-rate: 1e-5/s) | |
| Compressive strength (MPa) | 45.6 |
| Tensile strength from direct tensile tests (MPa) | 3.7 |

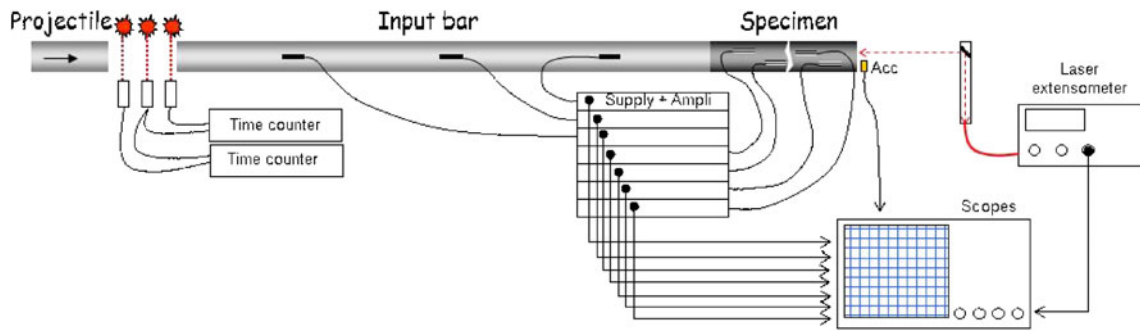


Fig. 1 Experimental device (projectile, input bar, specimen) and instrumentation (light sources, photo-diodes, strain gauges, accelerometer, and laser extensometer)

along the specimen until the free end where it is reflected as a tensile pulse that propagates in the opposite direction ($\sigma_t = g(x + C_0 \cdot t)$ in Fig. 2). Both signals interact such as ($\sigma(x, t) = \sigma_c + \sigma_t$) and ($\sigma(x_{free\ end}, t) = 0 \forall t$). When the tensile pulse exceeds the compressive pulse in amplitude, dynamic tensile loading spreads out the specimen leading to a possible failure of the concrete.

The Hopkinson bar made of high-strength aluminium alloy ($\sigma_y > 450$ MPa) is 1.2 m long and has a diameter of 45 mm. Three strain gauges are used on the bar to observe the incident and reflected pulses and to check the quality of the contact on the Hopkinson bar – specimen interface. The data of strain gauges are amplified (amplifier gain: 200) and recorded with a scope with the time base set to $0.1 \mu s$. The projectiles, made of the same aluminium alloy as the Hopkinson bar, are 70 or 80 mm long. Light sources coupled to infrared sensors, optical fibres and time counters allow evaluating the impact velocity of the projectile (Fig. 1).

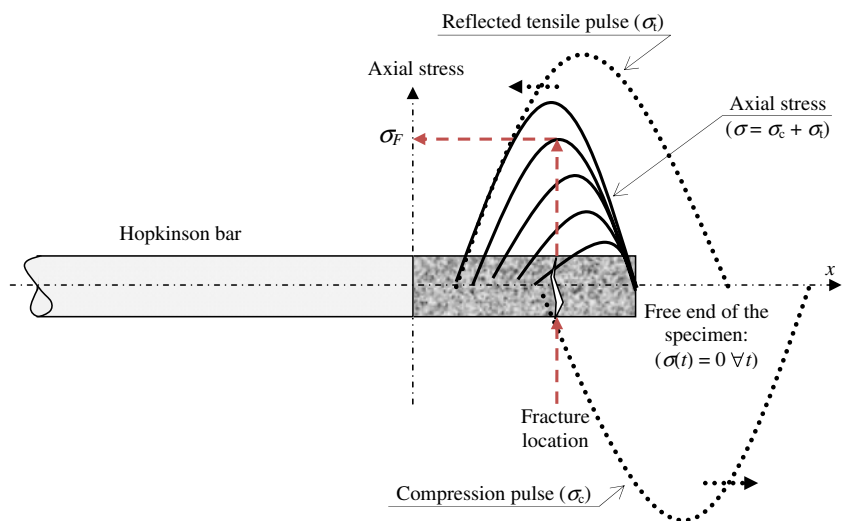
Strain gauges and a laser extensometer are also used. As explained below, the data are used to determine the level of strain-rate and the spall strength. The laser device, acting

like a VISAR, is directed towards the free end of the specimen to record the particle velocity. A series of tests was carried out involving the Hopkinson bar without specimens instrumented by the 3 strain gauges (Fig. 1) and an accelerometer (2.5 g , maximum acceleration: $600,000\text{ m.s}^{-2}$) on the free end besides the laser. For low impact velocities (few m/s), the difference observed between each measurement was less than 3%, which validates the whole instrumentation. However, the accelerometer suffers from several limitations, especially when it is applied to a concrete specimen, namely, it may perturb the local velocity field and set out or locally fail the specimen during the deceleration phase. This is why the laser extensometer was used in all tests performed on concrete specimens.

Optimization of the Compressive Pulse

Several pulse shaping techniques for testing materials at high rates of strain using Hopkinson bars are reported in the literature: from thin disks of annealed or hard copper placed between the projectile and the incident bar [21] to more

Fig. 2 Method A to process data for spalling tests: axial stress ($\sigma(x, t)$) corresponds to the superposition of the compressive pulse (σ_c) and the reflected tensile pulse (σ_t). The dynamic tensile strength (σ_F) is defined as the level of the elastic stress when the maximum value of stress is reached at the location of fracture



complex systems including for instance a flange attached to the impact end of the incident bar associated to a rigid mass [22] or two strikers separated by an elastic tube designed to obtain a double loading [23]. In every case, the aim is the optimization of the incident wave to master the testing

conditions. In this study, regarding the low impact velocities (about 6–11 m/s) hemispheric smooth-end projectile has been used. This simple technique allows obtaining a reproducible loading pulse and reducing the influence of the defect of parallelism at the striker –

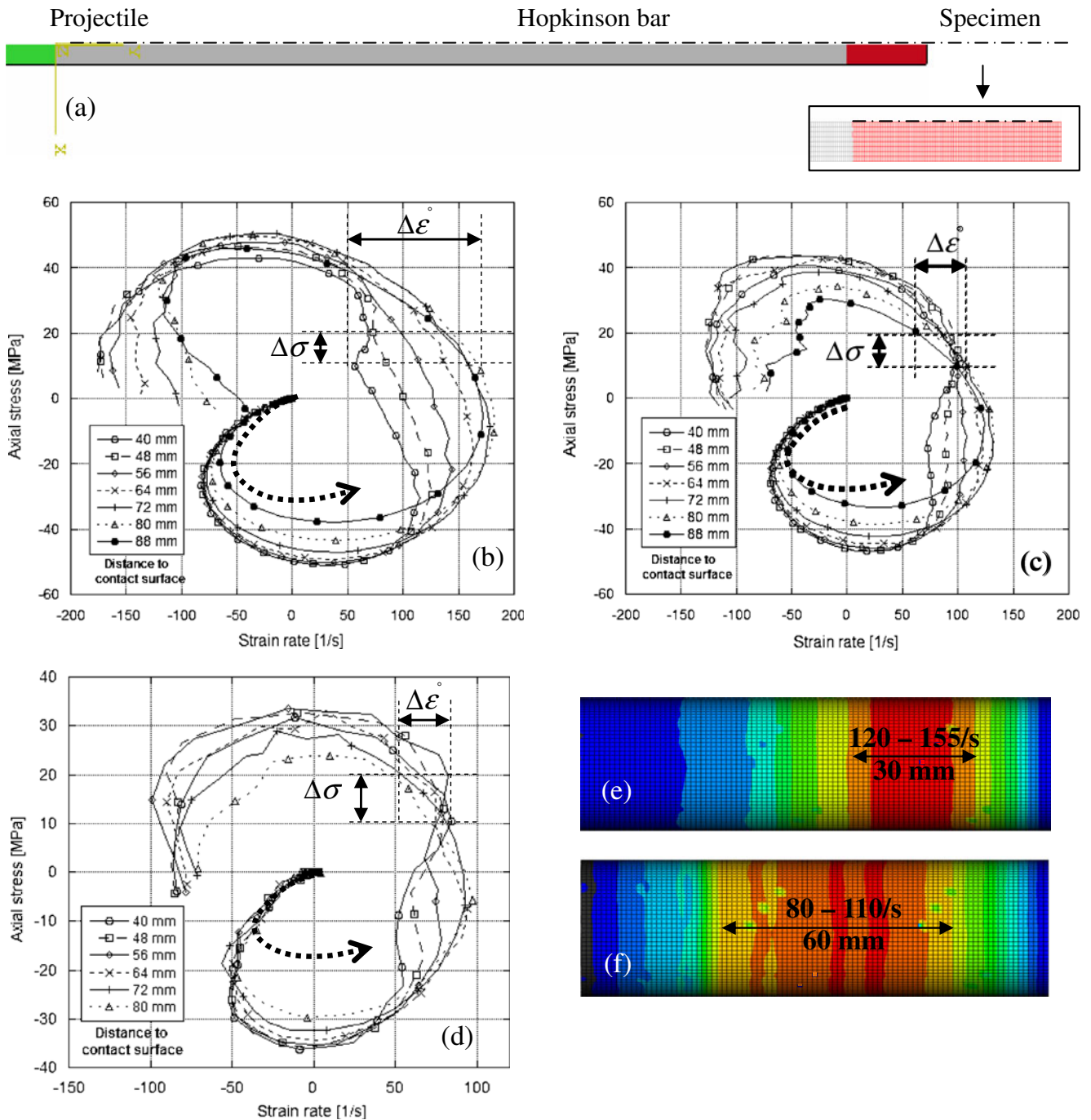


Fig. 3 Numerical simulations of a spalling test with an elastic model (specimen length: 120 mm). (a) Mesh used for the projectile, the Hopkinson bar and the specimen (Mesh size: 1mm), (b) results obtained for a flat-end projectile at $V_{\text{impact}}=10$ m/s, (c) results for the optimized geometry of projectile at $V_{\text{impact}}=10$ m/s, (d) results for the optimized geometry of projectile at $V_{\text{impact}}=6$ m/s, (e) and (f) field of strain-rate in the specimen respectively for a flat-end projectile and for the optimized geometry of projectile when maximum stress in the specimen reaches about 20 MPa

Hopkinson bar interface. Three smooth-end projectiles were evaluated from numerical simulations performed with the Abaqus/Explicit finite element code and assuming a purely elastic behaviour for the Hopkinson bar, the striker and the concrete specimen [Fig. 3(a)]. The specimen is discretized by axisymmetric elements of about 1 mm in length (9 280 elements). According to these computations, although the contact zone between the projectile and the Hopkinson bar is reduced, far away from the impact point the stress wave is quasi-plane: for instance, at the middle of the bar, the deviation of axial stress between the surface and the centre is less than 2% and the maximum deviation within the specimen is about 4%. Besides, the computations revealed a remarkable effect of the projectile geometry on the stress field in the specimen. For example, Fig. 3(b) shows the stress field in the concrete specimen considering a flat-end projectile impacting the input bar at 10 m/s. This plot shows the change of axial stress versus strain-rate. The most useful part of the plots corresponds to positive strain rates and the range of stress between 10 and 20 MPa. Inside the rectangle in dashed line, the strain-rate appears heterogeneous when a flat-end projectile is used (50/s – 180/s). With such loading, data processing may involve a strong uncertainty in the level of strain-rate and stress at failure. Several configurations were tested (3 radii of the hemispheric projectile-end and 3 impact velocities) to determine the best projectile shape with the aim to generate a tensile loading as homogeneous as possible on a widest part of the tested cylinder. Figure 3(c) shows results of a numerical simulation with the selected smooth-end projectile (radius of the hemispheric surface: 1.69 m) impacting the input bar at 10 m/s. Figure 3(d) presents the result obtained with the same geometry for an impact velocity of 6 m/s. In both cases, the strain-rate is quite well homogeneous in the range of stress from 10 to 20 MPa. The fields of strain rate obtained with both projectiles for a maximum stress in the specimen of 20 MPa are illustrated in Fig. 3(e) and (f). Again the relevance to use the optimized projectile is clearly observed.

Three Methods to Deduce the Spalling Strength

Several techniques have been proposed to evaluate the spall strength of concretes. Three of them are discussed below. In the first one –named method A–, the incident and reflected waves are shifted to the bar-specimen interface to rebuild the compressive pulse (σ_c) transmitted to the specimen. Next, the stress field in the sample is reconstructed as a function of time. The dynamic tensile strength is defined as the level of the elastic tensile stress reached when the maximum value of stress is reached at the location of fracture (cf. Fig. 2). This method was used by Klepaczko and Brara [9], Wu et al. [24] for spalling tests of concretes and by Gálvez et al. [25] for spalling of long bar made of ceramic. However, several

criticisms may be expressed, namely, the strength is deduced considering that, at the failure time, the state of stress in the specimen corresponds to a pure superposition of elastic waves (incident and reflected waves) without influence of the failure process itself. However, as explained by Grady and Kipp [26], Denoual and Hild [27], Hild et al. [28], and Forquin and Hild [29,30], due to a limited cracking velocity, the kinetics of damage in brittle or quasi-brittle materials is bounded and at the failure time the ultimate macroscopic stress (i.e. damaged stress) might not correspond to the microscopic stress (i.e. stress level without failure process). Moreover, the method is based on an accurate localization of fracture. However, according to post-mortem studies of spalling tests (see ref. [13] or picture shown below), damage may spread over a large area of several centimetres in width. Last, to be effective, the method would need a fast displacement of the point corresponding to the stress peak (cf. Fig. 2). As explained by Gálvez et al. [25], this may be difficult to obtain with pulses generated from cylindrical projectiles.

A second method (B) was introduced by Klepaczko and Brara [9]. In this method, the residual velocity of fragments is measured from successive pictures of a CCD video camera. Next, the spall strength is deduced from the following equation derived from a one-dimensional elastic-wave analysis:

$$\sigma_F = \rho C_0 V_{ejection}, \quad (1)$$

where ρ is the concrete density, C_0 the one-dimensional wave velocity, and $V_{ejection}$ the velocity of separation of

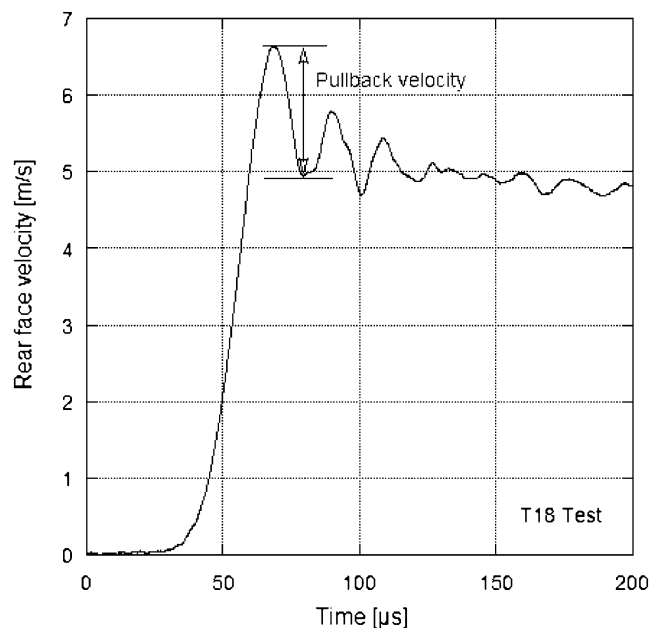
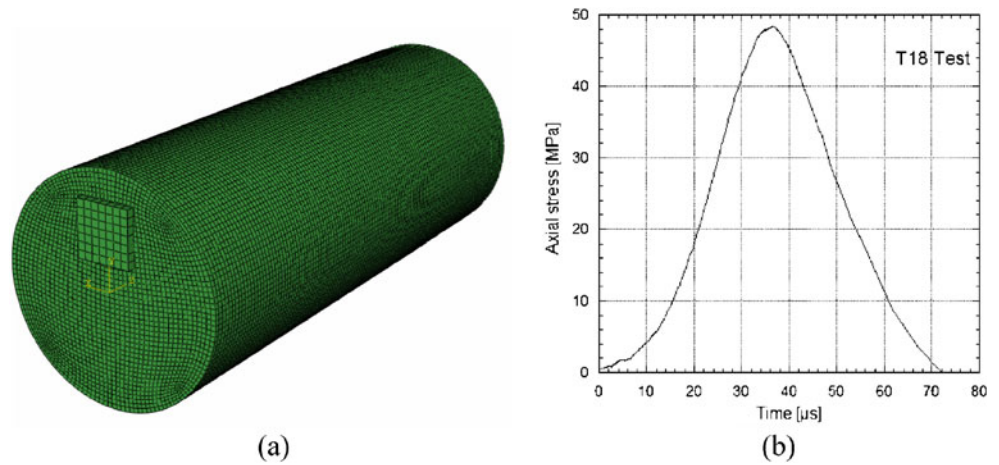


Fig. 4 Particle velocity at the rear face of the specimen versus time deduced from the laser extensometer measurement (T18 test). The pullback velocity “ ΔV_{pb} ” is defined as the difference in velocity between the maximum value and the velocity at rebound

Fig. 5 Numerical simulations of a spalling test. (a) Mesh used; (b) applied compression pulse (from data of T18 test)



fragments [9]. However the authors used the residual and stabilized velocity of each fragment instead of the particle velocity at the instant of failure on both sides of the failure plane. However, at the instant of failure the particle velocity is not necessarily homogeneous along the specimen. Moreover, in a case of a diffuse damage process, the material does not longer behave elastically in the damaged zone and the one-dimensional elastic-wave equation could not longer apply.

The third method (C) is derived from spalling tests performed on metals by the plate-impact technique. It has been applied previously by Schuler et al [10] to concrete specimens. Novikov et al. [11] introduced a linear acoustic approximation to obtain the spall strength from the velocity recorded on the rear face of the specimen:

$$\sigma_F = \frac{1}{2} \rho C_0 \Delta V_{pb}, \tag{2}$$

where “ ΔV_{pb} ”, called the pullback velocity, is the difference of the velocity between the maximum value and the velocity at rebound (cf. Fig. 4). However, it is assumed that the material still behaves elastically in between the cracking plane that initiates the rebound and the rear face. This point will be discussed in “Post Mortem Analysis of Failure Pattern” section. These 3 methods have been used in the literature but their ability to provide the spalling strength has to be checked. To do so, a series of numerical simulation have been conducted to discuss the validity of each approach.

Discussion of the Methods by Means of Numerical Simulations

Numerical simulations of the spalling test were performed with the Finite Element code Abaqus/Explicit to study the validity and accuracy of each method. The concrete cylinder (46 mm in diameter and 120 mm in length) was

thinly meshed by 3D elements of about 1 mm³ [Fig. 5(a)] and loaded by one of the highest compression pulses measured during the experiments [Fig. 5(b), T18 test]. As method A is based on a fast displacement of the stress peak, this point has been checked with a computation considering an elastic model for the specimen. In Fig. 6, the stress field

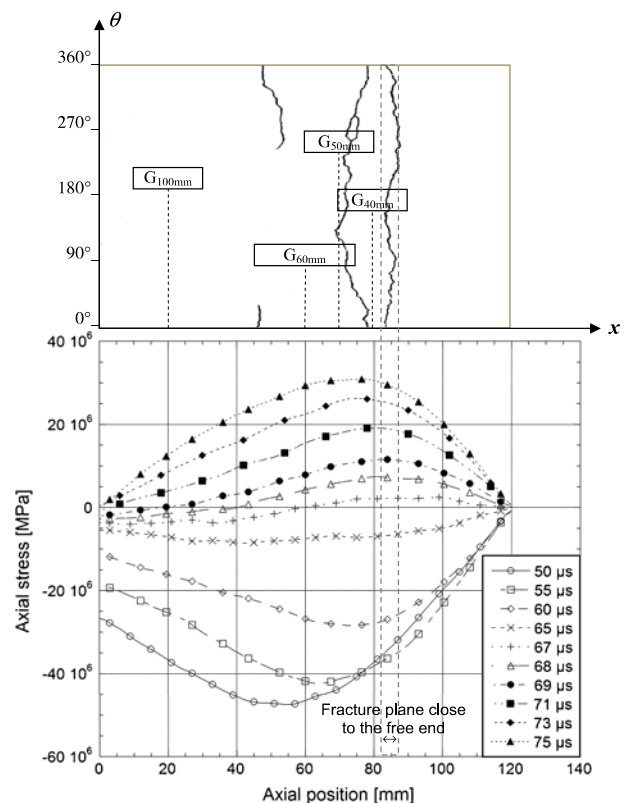


Fig. 6 Upper part: location of the main fracture planes in T18 specimen (length: 120 mm). Lower part: change of the axial stress field for distinct instants (numerical simulation of T18 test, elastic model). Applying method A, from the axial location of the fracture plane one deduces that the dynamic strength of T18 is in the range of 0 to 20 MPa

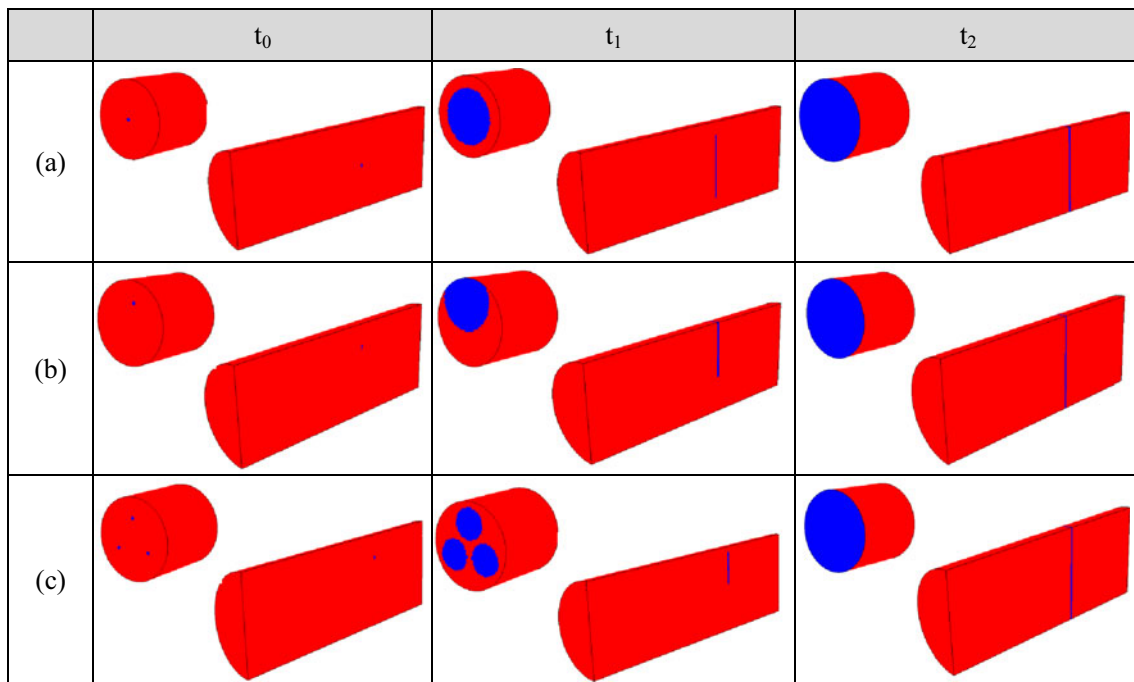


Fig. 7 Eroded part of the specimen at three instants for three different defect configurations. (a) A single defect is activated at the centre of the section, (b) a single defect is activated at $R/2$ from the axis, (c) three defects at 120° are activated at a distance $R/2$ from the axis

along the specimen axis is plotted at several instants (from $50\ \mu\text{s}$ to $75\ \mu\text{s}$). On the one hand, a fast increase of the stress level is observed (stress rate about $5\ \text{MPa}/\mu\text{s}$). On the other hand, the motion of the stress peak is very small between $67\ \mu\text{s}$ – $71\ \mu\text{s}$. Thus, according to axial location of the fracture plane (82 – $88\ \text{mm}$, upper part of Fig. 6), one might merely conclude that the dynamic strength of the specimen would be in the range of 0 to $20\ \text{MPa}$.

To evaluate methods B and C numerical simulations have been led based on an erosion technique. A user subroutine (called VUMAT) was developed to simulate the propagation of a single crack or multiple cracks in a unique fracture plane in the specimen. The point of initiation of cracks and the crack speed were arbitrarily defined. The

crack fronts correspond to circles, centred on the inception points and perpendicular to the axis of the specimen. For each numerical simulation, the ultimate strength was computed as the maximum value of the average axial stress in the eroded section. Different locations of inception, cracking velocities, and number of cracks were considered to evaluate the accuracy of each method in measuring the spall strength. Three cases are shown in Fig. 7.

Method B is based on the difference of velocity [equation (1)] whereas method C is based on Novikov et al. [11] formula [equation (2)]. Both methods were compared for several configurations of single and multiple fragmentations. The results are presented in Table 2. Method C based on the linear acoustic approximation of

Table 2 Comparison of methods B and C. Modelling of spalling tests with an erosion technique applied to a unique fracture plane

| Configuration | Fracture plane / free end [mm] | Crack velocity [m/s] | Ultimate strength [MPa] | Method C – (Equation (2)) [MPa] | Deviation [%] | Method B – (Equation (1)) [MPa] | Deviation [%] |
|--|--------------------------------|----------------------|-------------------------|---------------------------------|---------------|---------------------------------|---------------|
| 1 centred defect (case (a), Fig. 6) | 45 | 760 | 31.9 | 33.0 | 3.5 | 31.8 | 0.2 |
| 1 centred defect | 60 | 760 | 34.3 | 35.6 | 3.8 | 39.7 | 15.7 |
| 1 centred defect | 45 | 1,000 | 29.0 | 29.9 | 3.0 | 44.9 | 54.6 |
| 1 centred defect | 45 | 1,520 | 23.2 | 25.5 | 9.9 | 64.6 | 178 |
| 1 defect at radius/2 (case (b), Fig. 6) | 45 | 760 | 30.9 | 31.8 | 2.9 | 36.9 | 19.3 |
| 3 defects (120°) at radius/2 (case (c), Fig. 6) | 45 | 760 | 27.5 | 26.8 | 2.4 | 48.6 | 76.9 |
| 3 defects (120°) Radius / 2 | 35 | 760 | 24.7 | 24.2 | 2.0 | 45.9 | 85.7 |

Table 3 Comparison between methods B and C. Modelling of spalling tests with an anisotropic damage law

| Mesh | m | σ_0 [MPa] | Σ_u [MPa] | Method C – (Equation (2)) [MPa] | Deviation [%] | Method B – (Equation (1)) [MPa] | Deviation [%] |
|---------------|----|------------------|------------------|---------------------------------|---------------|---------------------------------|---------------|
| Coarse (4 mm) | 5 | 23.1 | 13.7 | 14.0 | 1.9 | 60.1 | 339 |
| Coarse (4 mm) | 10 | 19.1 | 13.7 | 13.6 | 1.0 | 65.6 | 379 |
| Coarse (4 mm) | 20 | 16.7 | 13.7 | 13.1 | 4.2 | 64.5 | 371 |
| Fine (1 mm) | 10 | 19.1 | 13.7 | 13.15 | 4.0 | 64.7 | 372 |

Novikov et al. [11] shows a good match with the ultimate strength in each configuration whereas predictions from method B are seen hazardous.

In the previous computations, a single fracture plane was considered to simulate failure. However, as shown below in a post-mortem study, numerous cracks may initiate during a spalling test. Therefore, one may ask whether the conclusions (i.e. good predictions with method C) might be extended to cases of diffuse damage. As the aim of the numerical simulations is only to check methods B and C, a simple evolution law of damage $D_i(\sigma_i)$ was used for each principal direction (\mathbf{d}_i) associated with the eigen microscopic stress (σ_i) and was integrated in a VUMAT subroutine:

$$D_i = 1 - \exp\left(-\left(\frac{\langle\sigma_i\rangle}{\sigma_0}\right)^m\right), \quad (3)$$

where $\langle\sigma_i\rangle$ is the positive part of the first ($i=1$), the second ($i=2$) or the third ($i=3$) eigen microscopic stresses, m and

σ_0 are constant parameters. Cracking in mode I induces only a compliance increase in the normal direction to the crack plane [27]. Therefore the macroscopic stress tensor Σ is related to the strain tensor ε by:

$$\varepsilon = \underline{\underline{K}}(D_1, D_2, D_3) \Sigma = \frac{1}{E} \begin{pmatrix} \frac{1}{1-D_1} & -\nu & -\nu \\ -\nu & \frac{1}{1-D_2} & -\nu \\ -\nu & -\nu & \frac{1}{1-D_3} \end{pmatrix} \Sigma, \quad (4)$$

where E is Young's modulus, and ν Poisson's ratio of the undamaged material and the microscopic stress tensor is expressed as $\sigma = \underline{\underline{K}}^{-1}(0, 0, 0) \varepsilon$. Equation (3) allows one to obtain a constant ultimate strength for any strain-rate, which makes the comparison easier with predictions from methods B and C. In spalling tests, the damage variable (D_1) is associated with the axial direction and while it grows from 0 to 1 other damage variables remain very low

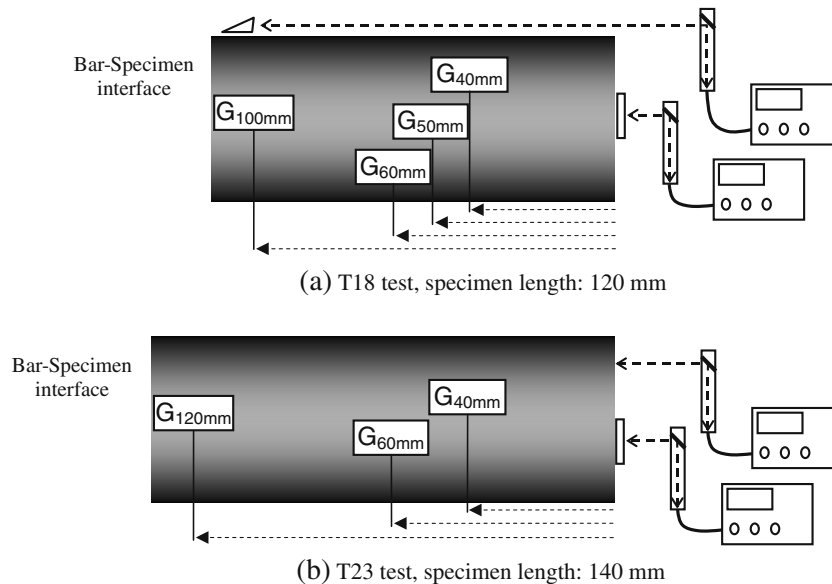


Fig. 8 Strain gauges and laser extensometers used in two tests. (a) T18 test: 4 strain gauges located 40, 50, 60, 100 mm from the free end. (b) T23 test: 3 strain gauges located 40, 50, 120 mm from the free end

($D_2 \approx 0$ and $D_3 \approx 0$). In that case $\Sigma_1 = (1 - D_1)\sigma_1$ and for any strain-rate, the ultimate strength reads:

$$\Sigma_u = \sigma_0 \left(\frac{1}{m.e} \right)^{\frac{1}{m}}. \quad (5)$$

Three Weibull moduli m and two mesh sizes were considered for the computations (Table 3). The reference stress σ_0 was selected to obtain an arbitrary ultimate strength Σ_u of 13.7 MPa in all the computations (the value 13.7 MPa corresponds approximately to the strength measured in T18 test detailed below). Parameters and ultimate strengths deduced from methods B and C for each numerical simulation are compared in Table 3. Again, method C shows a good match with the ultimate strength for any value m and mesh used, whereas method B gives significantly greater deviation especially in a case of diffuse and gradual damage as observed in post-mortem studies reported below.

Influence of Reflectors on the Measurement of Particle Velocity

Two kinds of reflectors made of aluminium alloy were used in the spalling tests to measure the particle velocity on the specimen surface with laser extensometers (triangles and thin tiles). The triangles were glued on the cylindrical surface of the specimen, whereas the thin tiles were glued on the rear face (Fig. 8, T18 test).

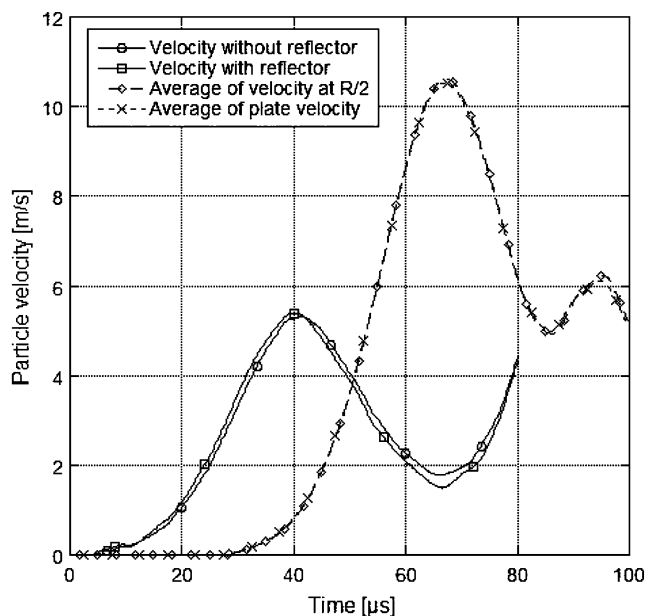


Fig. 9 Influence of reflectors (triangle and thin tile) in measuring the particle velocity (erosion process of case (c), Table 2). Solid line and square symbols: triangle reflector located 100 mm from the free end, dotted line and cross symbol: thin tile glued against the free end and located at a distance $R/2$ from the axis

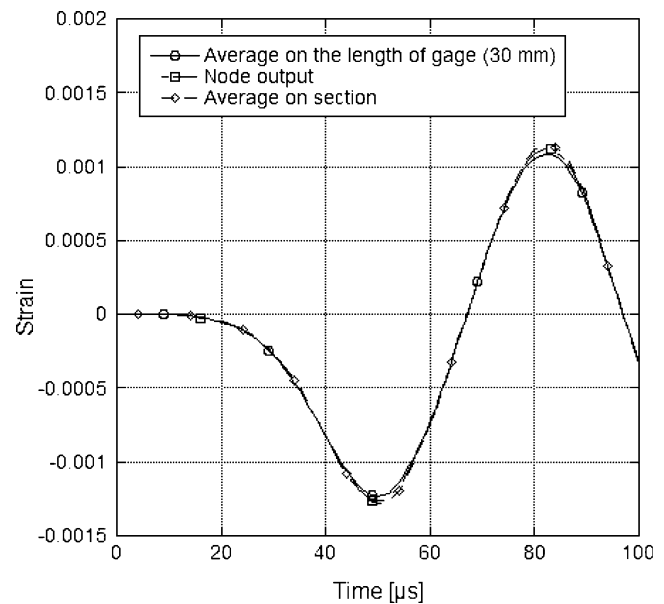


Fig. 10 Influence of a gauge length of 30 mm on the measurement of strain (numerical simulation of T18 test, elastic model, gauge: $G_{60\text{mm}}$). The maximum difference between the three curves is less than 5% in compression and less than 1% in tension for an elastic strain of 3.6×10^{-4} , namely, the strain corresponding to the dynamic strength of T18 test (13.7 MPa)

MB50 micro-concrete is a composite material made of a cement matrix and sand grains (with a maximum grain size of ca. 2 mm). Thus, large reflectors were used in most of the experiments, namely, the triangles (7 mm in length, 4.5 mm in height, mass: 0.17 g) and the thin tiles (cross-sectional area: 12 mm^2 , 1.6 mm in thickness, mass: 0.6 g) [Fig. 8(a)]. The thin tiles are located at a distance $R/2$ from the axis [cf. Fig. 5(a)]. In parallel to the experiments, a series of numerical simulations were performed to check whether the mass of the tiles and triangles may influence the velocity signals. For the computation, mesh and compression loading of Fig. 5 were considered as well as the erosion process of case (a) (Table 2, Fig. 7). The particle velocities deduced from both numerical simulations (i.e. with and without aluminium reflectors) are plotted in Fig. 9. It is observed that the error due to the use of reflectors in measuring the particle velocity peak is less than 2% for a triangle and less than 1% for a thin tile glued on the free end. According to equation (2), the corresponding error to evaluate the dynamic strength does not exceed about 0.3 MPa. This result was confirmed by several tests performed with two laser extensometers in configuration T23 [see Figs. 8(b) and 12].

Influence of Gauge Length on the Measurement of Strain

The numerical simulations presented in Fig. 5 (elastic model, incident pulse from T18 test) were also used to

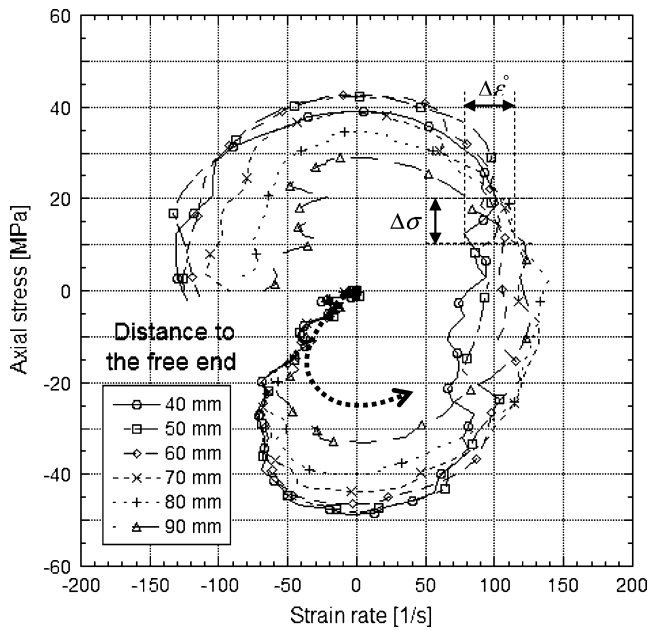


Fig. 11 Strain-rate as a function of the stress level (numerical simulation of T18 test, elastic model). In the 10–20 MPa stress range, the deviation of strain-rate is low

evaluate the influence of the length of the strain gauges. Figure 10 shows the change of axial strain given by one node placed at 60 mm from the free end [see Fig. 8(a)] compared to that of strain averaged on the length of the gauge (30 mm), and of the average axial strain in the whole section. The maximum difference between the three curves is less than 5% in compression and less than 1% in tension

for an elastic strain of 3.6×10^{-4} , namely, the strain corresponding to the dynamic strength (T18 test: 13.3 MPa). This result confirms the advantage of using strain-gauges in spalling tests without affecting noticeably the measurement when smooth-end projectiles are used. This conclusion is further supported if one considers the curves of Fig. 11. In the same way as in Fig. 2(c) and (d), the stress is plotted as function of strain-rate for axial coordinates between 40 and 90 mm with regard to the free end. Contrary to the simulations of Fig. 2, an experimental compressive pulse (T18 test) was applied to the specimen in the computation. In the useful part of the plot (positive stress and strain rate), when the stress reaches about 10 to 20 MPa, the curves are crossing each other. Thus, uniformity of the loading predicted in “Optimization of the Compressive Pulse” is expected in real tests at least until the onset of damage, which allows the use of strain gauges. This result was confirmed in several experiments by comparing signals from gauges located at different spots along the axis of the specimen. For instance, data from strain gauges located at 40, 50, 60 mm from the rear face are remarkably superimposed from time $t = -10 \mu s$ until the failure time (2.5 μs) i.e. when the axial stress evolves from -40 MPa to 13.3 MPa [Fig. 13(a)].

Data Processing

Wave Speed, Dynamic Young's Modulus and Spall Strength

The instrumentation used in the experiments (Fig. 8) allows one to obtain various data. First, the location of strain

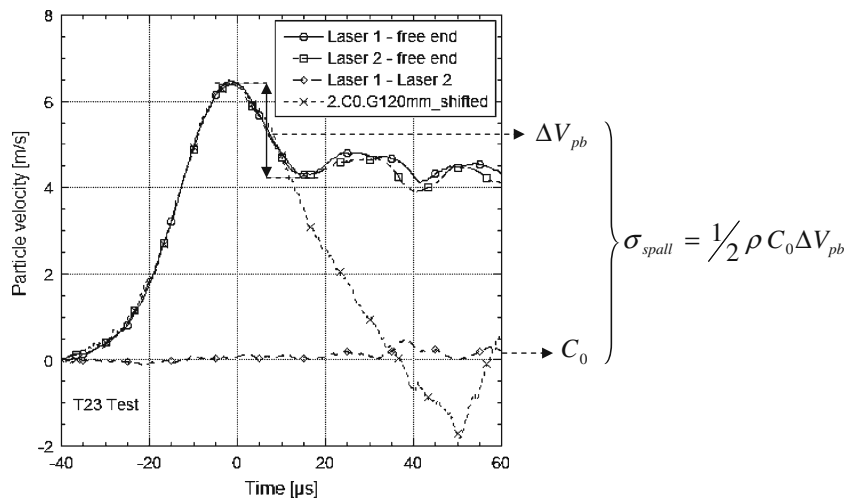


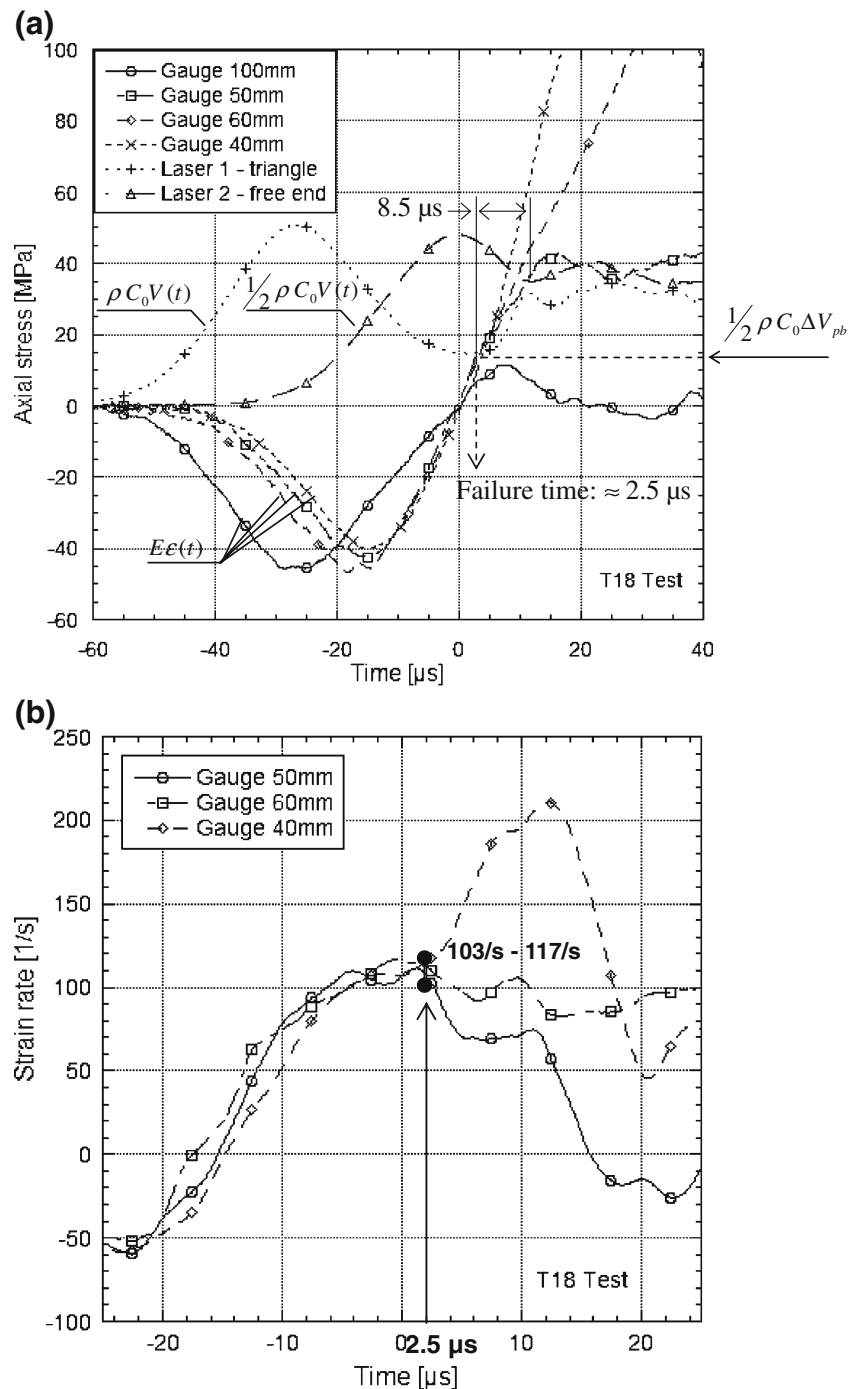
Fig. 12 Gauge signal from G_{120mm} is shifted to find the wave speed. The pull-back velocity is obtained from data of laser extensometers. Next, the spall strength is deduced

gauges being known, the 1D wave speed C_0 is derived from the difference between the time corresponding to the minimum value of strain of the first gauge placed on the specimen ($G_{100\text{mm}}$ or $G_{120\text{mm}}$, Fig. 8) and the time corresponding to the maximum value of velocity measured by the laser (cf. Fig. 12). Next, the spall strength is deduced

according to equation (2). Furthermore, dynamic Young's modulus is estimated from C_0 :

$$C_0 = \sqrt{\frac{E_{dyn}}{\rho}} \Rightarrow E_{dyn} = \rho C_0^2 \tag{5}$$

Fig. 13 Method to deduce the strain rate of T18 test: the spall strength is deduced from the pull-back velocity obtained from data of laser 2 [Fig. 13(a)]. According to Fig.7, the main fracture plane is located 40 mm from the free end. Therefore, Gauge $G_{40\text{mm}}$ is used to obtain the failure time ca. $2.5\mu\text{s}$ [Fig. 13(a)]. Next, the strain rate at failure time is deduced, namely, ca. $103\text{--}117/\text{s}$ [Fig. 13(b)], (a) Data obtained in T18 test converted in stress level: $E \cdot \varepsilon(t)$ for data of strain gauges $G_{40\text{mm}}$, $G_{50\text{mm}}$, $G_{60\text{mm}}$, $G_{100\text{mm}}$ [cf. Fig. 8(a)], $\rho C_0 V(t)$ for Laser 1 (triangle reflector) and $\frac{1}{2}\rho C_0 V(t)$ for Laser 2 (free end). The dynamic strength being known, the signal from gauge $G_{40\text{mm}}$ is used to identify the “failure time” (b) Signals (from gauges 40, 50, 60 mm from the free end) are time-derived. The “failure time” being known, the signals delivered by gauges $G_{40\text{mm}}$, $G_{50\text{mm}}$, $G_{60\text{mm}}$ are used to evaluate the strain-rate at failure



The mean values obtained for the wave speed and the dynamic Young's modulus of wet MB50 are respectively 4062 m/s and 37.95 GPa.

Strain-rate

Spall experiments are complex because stresses evolve continuously and fast. First, a “failure time” is defined according to the method reported in Fig. 13(a). The dynamic strength being known, the gauge signal is used to identify accurately the “failure time”. Next, gauge signals are time-derived to deduce the change of the strain-rate in the damaged area [Fig. 13(b)]. Last, the strain-rate at failure time is deduced (ca. 103–117/s for T18 test).

Experimental Results and Post Mortem Observations

Experimental Results

Fifteen wet specimens of MB50 micro-concrete were subjected to spalling tests with different impact velocities generating dynamic tensile loading for strain rates ranging from 30 to 150/s. In this range, the dynamic strength deduced from laser extensometer (equation (2)) varies from 11.7 MPa to 15.8 MPa. For the highest strain rate (150/s), the maximum compressive stress reached in the specimen –62 MPa and slightly exceeded the quasi-static compressive strength of MB50 concrete (45.6 MPa, Table 1) during 15 μ s. However, the compressive strength of wet concrete is

Table 4 Results of spalling tests on the wet MB50 micro-concrete

| Specimen | Strain rate at failure [1/s] | Spalling stress [MPa] |
|----------|------------------------------|-----------------------|
| T3 | 31 | 11.7 |
| T5 | 51 | 12.8 |
| T6 | 99 | 13.3 |
| T7 | 72 | 12.4 |
| T11 | 153 | 15.3 |
| T14 | 140 | 14.4 |
| T15 | 130 | 15.8 |
| T16 | 78 | 14.3 |
| T17 | 59 | 13.6 |
| T18 | 105 | 13.3 |
| T25 | 145 | 14.4 |
| T26 | 105 | 14.8 |
| T27 | 115 | 14.0 |
| T28 | 160 | 14.9 |
| T46 | 121 | 15.0 |
| T45 | 41 | 12.9 |

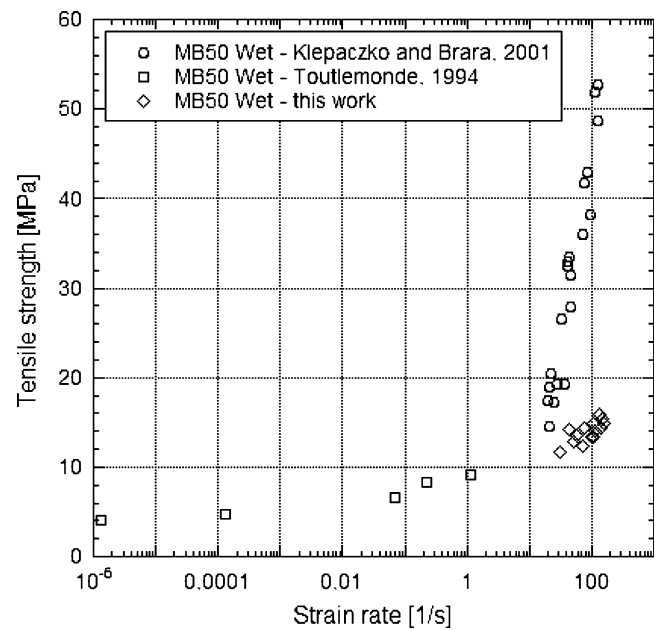


Fig. 14 Comparison of the experimental results obtained in this work (method C) with data from Klepaczko and Brara [9] (methods A and B) and from Toutlemonde [4]

known to increase significantly at high strain-rates (dynamic increase factor about 2 at strain-rate of 100/s) [16,31,32]. Moreover, post-mortem studies did not reveal any characteristic compressive damage as axial cracks. Thus, the compressive loading is assumed to have no consequence on the spall strength. The results are reported in Table 4 and are compared to the values obtained with methods A and B

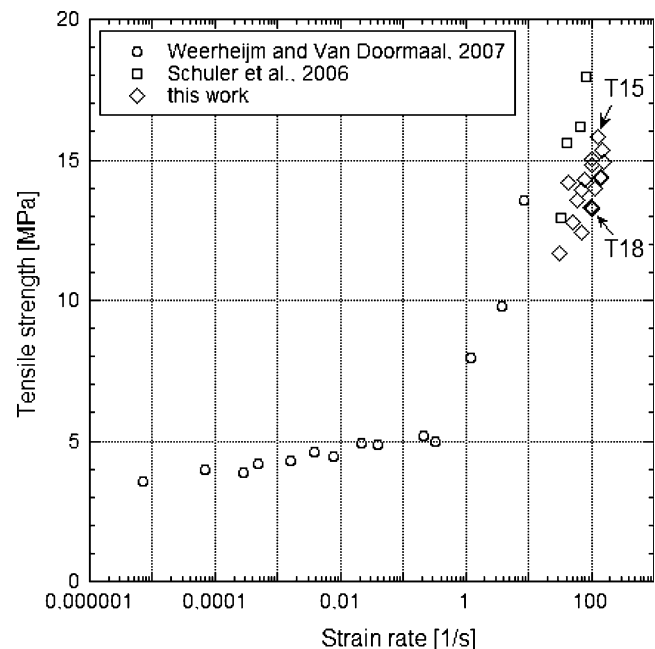


Fig. 15 Comparison of the experimental results obtained herein with data obtained for two other concretes [10,13]

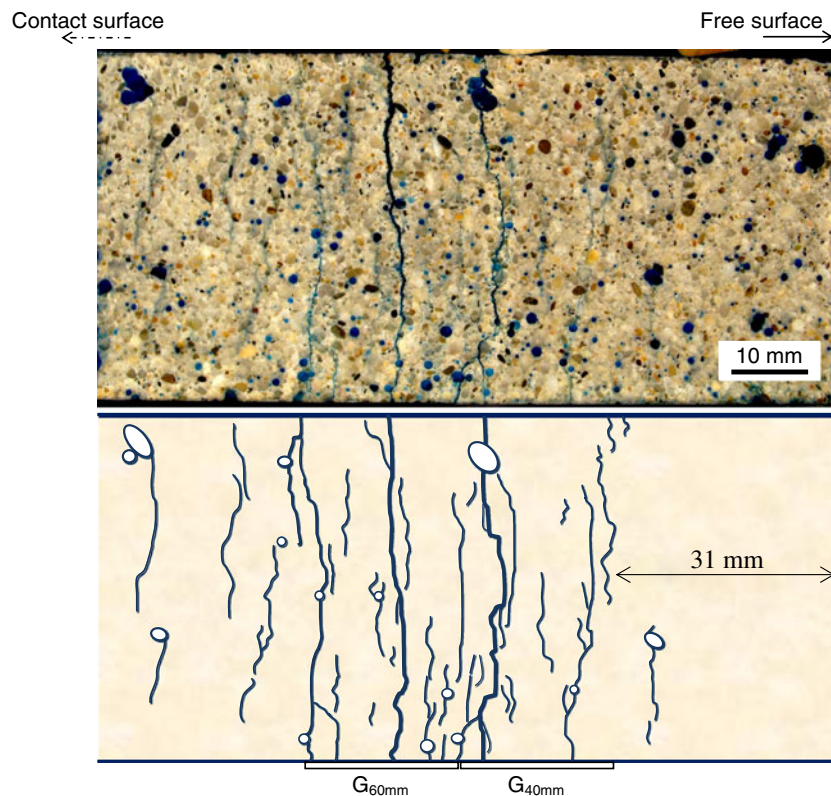


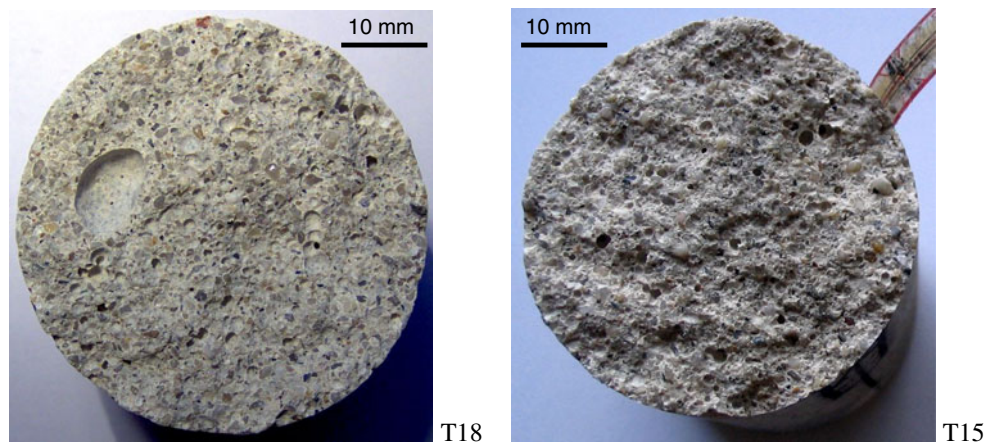
Fig. 16 Post-mortem observation of failure pattern (T15 test, specimen length: 140 mm, strain rate: 130/s) and position of gauges G_{40mm} and G_{60mm} . The specimen is infiltrated with a coloured hyper-fluid resin, cut and finely polished. The cracks are spread over a large area (approximately 70 mm in length)

(Three Methods to Deduce the Spalling Strength) by Klepaczko and Brara [9] with MB50 concrete (Fig. 14). Both methods lead to strongly different results especially concerning data obtained at the highest rates of strain. Nevertheless, the same deviation of strength was observed between both methods B and C in FEM analysis involving the damage model (cf. Table 3).

Comparison with Data Obtained with Other Concretes in the Literature

The results are also compared to data of spalling tests reported by Schuler et al. [10], and Weerheijm and Van Doormaal [13] (cf. Fig. 15). In these works analogous experimental techniques are used (i.e. concrete specimen

Fig. 17 Post-mortem observation of the main fracture plane of tests T18 and T15. For sample T18, a large pore is seen whereas only small pores are observed for sample T15



loaded through a Hopkinson bar apparatus). Moreover the quasi-static tensile strength of the tested concretes (about 3 MPa) is similar to that of MB50 micro-concrete (3.7 MPa, Table 1). In addition, these authors used direct measurement applied to the specimen to determine the dynamic tensile strength: Weerheijm and Van Doormaal [13] employed a series of strain gauges on long specimens whereas Schuler et al. [10] glued an accelerometer on the free end of the specimen. Although the size of specimens and the microstructure of concretes differ, the difference of strength does not exceed about 4 MPa for a given strain-rate.

Post Mortem Analysis of Failure Pattern

It was observed that depending on the loading-rate, the failure pattern of the specimens might vary considerably. Below 50/s, the specimen was usually recovered intact (without any fractured planes). However, bounce of particle-velocity on the free end as well as important residual strains detected in strain-gauges point-out the occurrence of damage in the specimen. Between 50/s – 90/s, a single fracture plane was mostly observed whereas two or three fracture planes generally occurred above 100/s. For example, in test T18, three planes of cracking were observed at 34, 50 and 68 mm from the free end of the specimen. However, several specimens infiltrated with a coloured hyper-fluid resin, cut and finely polished revealed additional short cracks (few centimetres in length) that developed in the specimen parallel to the main fracture planes. For example, by using an optical microscope, around forty distinct cracks have been observed on failure pattern of T15 sample (reported on Fig. 16). In addition, from experimental data of T15 test it is observed that the time interval between the failure time and the time at rebound is precisely equal to $7.8\mu\text{s}$ [$8.5\mu\text{s}$ for T18 specimen, see Fig. 13(a)]. $7.8\mu\text{s}$ is the time needed to cover 32 mm at the 1D wave speed C_0 . Now, this distance may be compared to the axial location of the closest cracking plane toward the rear face (31 mm, Fig. 16). Thus, the rebound is due to the nearest crack with regard to the specimen end. Consequently, one may assume that the material still behaves elastically in between the cracking that induced the rebound and the rear face and the Novikov's formula based on 1D-elastic wave propagation is valid.

The main fracture planes were also examined (Fig. 17). Almost no aggregate breakage is observed, probably due to their small size (i.e. about 2 mm). Moreover, in several fracture planes, a large porosity is seen as, for instance, in sample T18 (pore 7 mm in diameter, Fig. 17) whereas this phenomenon is not observed in other fracture planes (sample T15, Fig. 17). In both cases (triggered or not on a large pore), the dynamic strength varied less than 2 MPa, a

confirmation that a single defect may not control the whole failure at high rates of strain.

Conclusion

Spall experiments are difficult tests because of the complexity in time and space of the transient loading. In the present work, several numerical simulations were carried out to improve the analysis and understanding of the spalling tests. First, smooth-end projectiles were designed to optimize the incident pulse and to control the distribution of stress in the specimen in axial direction. According to experimental and numerical results, an enhanced uniformity of the strain rate was obtained for positive stresses in the range of 10 to 20 MPa in which the dynamic strength is observed. One may use strain gauges in the damaged area to improve the direct evaluation of the strain rate. According to finite element calculations, the length of strain gauges did not affect significantly the measured value. Furthermore, three methods to identify the dynamic tensile strength have been discussed. Numerical results showed that the linear acoustic approximation introduced by Novikov et al. [11] is valid when applied to spall experiments, whereas methods based on the location of the fracture plane or the velocity of separation of fragments might lead to erroneous results. Moreover, small reflectors such as thin tiles may be used to average the local field of the particle velocity on the free surface. Fifteen wet specimens of MB50 micro-concrete were subjected to tensile loading at high strain rates (30–150/s), and a dynamic strength of about 12 to 16 MPa was obtained. Post-mortem observations revealed that at high strain-rate failure is the consequence of numerous oriented cracks initiated or not on large pores and the rebound of velocity on the rear face is likely due to one of the nearest crack with regard to the specimen end.

Acknowledgments The authors are grateful to I. Vegt from TNO, Professor F. Hild from LMT-Cachan, Professors J.R. Klepaczko and L. Toth from LPMM and to Délégation Générale pour l'Armement - Centre d'Etudes de Gramat for supporting this work.

References

1. Goldsmith W, Polivka M, Yang T (1966) Dynamic behavior of concrete. *Exp Mech* 6(2):65–79
2. Birkimer DL, Lindermann R (1971) Dynamic tensile test of concrete materials. *ACI J* 68(8):47–49
3. Malvar LJ, Ross CA (1998) Review of strain rate effects for concrete in tension. *ACI Mater J* 95(6):735–739
4. Toutlemonde F (1994) Ph.D. thesis: Résistance au choc des structures en béton : du comportement du matériau au calcul des ouvrages. LCPC, Paris

5. Rossi P (1991) A physical phenomenon which can explain the material behaviour of concrete under high strain rates. *Mater Struct* 24:422–424
6. Körmeling HA, Zielinski AJ, Reinhardt HW (1980) Experiments on concrete under single and repeated uniaxial impact tensile loading. *Stevin Report* 5-80-3, Delft
7. Zielinski AJ (1982) Ph.D. thesis: fracture of concrete and mortar under uniaxial impact tensile loading. Delft University of Technology
8. McVay MK (1988) Spall damage of concrete structures. Technical Report SL-88-22, US Army Corps of Engineers, Waterways Experiment Station, Vicksburg, Miss., USA
9. Klepaczko JR, Brara A (2001) An experimental method for dynamic tensile testing of concrete by spalling. *Int J Impact Eng* 25:387–409
10. Schuler H, Mayrhofer C, Thoma K (2006) Spall experiments for the measurement of the tensile strength and fracture energy of concrete at high strain rates. *Int J Impact Eng* 32:1635–1650
11. Novikov SA, Divnov II, Ivanov AG (1966) The study of fracture of steel, aluminium and copper under explosive loading. *Fizika Metallov i Metallovedeniye* 21(4)
12. Vegt I, Weerheijm J (2006) Dynamic response of concrete at high loading rates. A new Hopkinson bar device. In *Proc Int Symp. Brittle Matrix Composites 8*, Warsaw
13. Weerheijm J, Van Doormaal JCAM (2007) Tensile failure of concrete at high loading rates: new test data on strength and fracture energy from instrumented spalling tests. *Int J Impact Eng* 34:609–626
14. Forquin P (2003) Ph.D. thesis: Endommagement et fissuration de matériaux fragiles sous impact balistique, rôle de la microstructure. LMT, Cachan
15. Bernier G, Dalle JM (1998) Rapport d'essai de caractérisation des mortiers, Science Pratique S.A.
16. Gary G, Klepaczko JR (1992) Essai de compression dynamique sur béton, GRECO Geomaterial scientific report, 105–118
17. Gatuingt F (1999) Ph.D. thesis: Prévion de la rupture des ouvrages en béton sollicités en dynamique rapide. LMT, Cachan
18. Buzaud E (1998) DGA Centre d'Etudes de Gramat, Report: Performances mécaniques et balistiques du microbéton MB50
19. Forquin P, Gary G, Gatuingt F (2008) A testing technique for concrete under confinement at high rates of strain. *Int J Impact Eng* 35:425–446
20. Forquin P, Safa K, Gary G (2009) Influence of free water on the quasi-static and dynamic strength of concrete in confined compression tests, *Cement Con. Res.* Submitted for publication
21. Frew DJ, Forrestal MJ, Chen W (2001) Pulse shaping techniques for testing brittle materials with a split Hopkinson pressure bar. *Exp Mech* 42(1)
22. Song B, Chen W (2004) Loading and unloading split Hopkinson pressure bar pulse shaping techniques for dynamic hysteretic loops. *Exp Mech* 44(6)
23. Chen W, Luo H (2004) Dynamic compressive responses of intact and damaged ceramics from a single split Hopkinson pressure bar experiment. *Exp Mech* 44(3)
24. Wu H, Zhang Q, Huang F, Jin Q (2005) Experimental and numerical investigation on the dynamic tensile strength of concrete. *Int J Impact Eng* 32:605–617
25. Galvez Diaz-Rubio F, Rodriguez Perez J, Sanchez Galvez V (2002) The spalling of long bars as a reliable method of measuring the dynamic tensile strength of ceramics. *Int J Impact Eng* 27:161–177
26. Grady DE, Kipp ME (1980) Oil shale fracture and fragmentation at high rates of loading, SAND-76-0563C. Sandia Report
27. Denoual C, Hild F (2000) A damage model for the dynamic fragmentation of brittle solids. *Comp Methods Appl Mech Eng* 183:247–258
28. Hild F, Denoual C, Forquin P, Brajer X (2003) On the probabilistic-deterministic transition involved in a fragmentation process of brittle materials. *Comput Struct* 81(12):1241–1254
29. Forquin P, Hild F (2008) Dynamic fragmentation of an ultra-high strength concrete during Edge-On Impact tests, *ASCE Journal of Engineering Mechanics*. *ASCE J Eng Mech* 134(4):302–315
30. Forquin P, Hild F. A probabilistic damage model of the dynamic fragmentation process in brittle materials, *Advances in Applied Mechanics*, Submitted for publication
31. Bischoff PH, Perry SH (1991) Compressive behaviour of concrete at high strain rates. *Mater Struct* 24:425–450
32. Schmidt JM (2003) Ph.D. thesis: high pressure and strain-rate behaviour of cementitious materials: experiments and elastic/viscoplastic modelling. University of Florida, USA